Dalton Transactions

Versatile Functionalization of De-Fluorinated FMOF-1 Towards Enhanced Carbon Capture and Separation: A Predictive Molecular Simulation Study

Journal:	*Dalton Transactions*
Manuscript ID	DT-ART-11-2024-003093.R1
Article Type:	Paper
Date Submitted by the Author:	30-Jan-2025
Complete List of Authors:	Yasmeen, Rashida; University of North Texas, Department of Materials Science and Engineering Islam, Sheikh; University of North Texas, Department of Chemistry Du, Jincheng; University of North Texas, Material Science and Engineering Omary, Mohammad; University of North Texas, Chemistry

Versatile Functionalization of De-Fluorinated FMOF-1 Towards Enhanced Carbon Capture and Separation: A Predictive Molecular Simulation Study

Rashida Yasmeen[1], Sheikh M. S. Islam[2], Jincheng Du[1,*], and Mohammad A. Omary[2,*]

[1]*Department of Materials Science & Engineering, University of North Texas, Denton, Texas-76203, United States*

[2]*Department of Chemistry, University of North Texas, 1155 Union Circle, Denton, Texas-76203, United States*

*Corresponding Authors. Email: Omary@unt.edu (M.A.O.);
Jincheng.Du@unt.edu (J.D.)

ABSTRACT

Fluorous metal-organic frameworks, FMOFs, represent a superhydrophobic class of MOFs containing -CF_3 or -F groups in their pores. The primary objective of this research is to computationally design functionalized FMOF-1 with X = -OCH_3, -CN, -OH, -COOH and -NH_2 instead of -CF_3 and analyze their CO_2 adsorption and separation characteristics. Grand Canonical Monte Carlo (GCMC) simulations are used to study adsorption properties of CO_2, CH_4 and N_2 in all structures. Henry's constant (K_H) and isosteric heat of adsorption at infinite dilution (Q_{st0}) estimated from GCMC simulations plus the binding energy (BE) from Möller-Plesset second-order perturbation theory (MP2) quantum-mechanical simulations characterize adsorbate-adsorbent interaction strengths. Such simulations predict a systematic enhancement of all K_H, Q_{st0}, and BE values in X-functionalized MOFs vs the parent FMOF-1. Among such functional MOFs, the X = -COOH structure is predicted to exhibit the largest CO_2 uptake in the low-pressure region due to the strongest CO_2/-COOH interaction strength, as supported by the largest K_H (1.02×10^{-4} mol/kg/Pa). In contrast, at high pressures (30 bar), the X = -OH structure is predicted to exhibit the highest CO_2 uptake. Indeed, replacing the -CF_3 groups in FMOF-1 by any aforementioned X group is expected to afford higher CO_2 uptake in the GCMC-simulated adsorption isotherms compared to the parent material. The selective adsorption of CO_2 over CH_4 and N_2 was determined using the ideal adsorbed solution theory (IAST) method at 50:50 and 15:85 CO_2/CH_4 and CO_2/N_2 binary mixtures, respectively. The X = -COOH structure amounts to the largest selectivity (59.6 for CO_2/CH_4 and 128.7 in CO_2/N_2); i.e., nearly 40x and 43x higher vs FMOF-1 (1.5 and 3 in CO_2/CH_4 and CO_2/N_2, respectively) at 298 K and 0.1 bar. Functionalized MOFs for CO_2 separation, natural gas purification, landfill gas separation, and/or CO_2 flue gas capture suggest X = -OH, -COOH and -NH_2 are promising to enhance adsorption capacity and selectivity.

1. INTRODUCTION

Traditional porous materials such as silica, activated carbons, zeolites have been studied as a potential adsorbent for carbon capture and storage (CCS) for a while.[1,2] However, no materials have shown superior quality and bear the drawbacks of either low adsorption selectivity or smaller uptake capacity of CO_2.[3,4] In order to overcome the limitations of traditional porous solids, researchers have been exploring on metal organic frameworks (MOFs) extensively in the recent days, for the enhanced adsorption and separation of CO_2.[5–8] Having the quality of higher porosities and tunable chemical properties MOFs have shown remarkable potential for adsorptive separation, to date.[9–14] To achieve improved adsorption and selectivity of CO_2, the properties of MOFs could be tuned/ have been tuned in different ways such as by controlling pore sizes, incorporating alkali-metal cations, introducing open metal sites, etc.[15–17]

Ligand functionalization[18–22] is a potential approach for the improvement of adsorbate-adsorbent interaction, that could result in enhanced CO_2 adsorption in MOFs. Addition of different functional groups to a linker can significantly affect the CO_2 adsorption and separation capacities of the structures.[23,24] Arstad et al.[25] and An et al.[26] found that amine group can improve the CO_2 uptake in MOFs through the formation of larger binding sites compared to the parent MOFs. Couck et al.[27] incorporated amino group in MIL-53 (Al) and showed enhanced CO_2/CH_4 selectivity compared to the original MOF, MIL-53 (Al). Zhang et al.[28] reported higher isosteric heats of adsorption (Q_{st}) and improved CO_2 uptake in acylamide-decorated MOFs than that of the unfunctionalized structures. Improved Q_{st} was observed for amino functionalized MIL-53 (Al) as well with a value of □ 38.4 kJ/mol, whereas the Q_{st} value for the parent MIL-53 (Al) was < 20 kJ/mol.[27] Torrisi et al.[29,30] investigated the impact of functionalization on CO_2 adsorption by incorporating -OH, -COOH, $-NH_2$ and $-CH_3$ groups in MIL-53(lp). As per the work significantly

higher CO_2/CH_4 selectivity was predicted for -COOH and -OH functionalized MIL-53 (lp) compared to the parent MIL-53 (lp). Gu et al.[31] have used density functional theory (DFT) to study the effects of functional groups for the improvement of CO_2 uptake by introducing -SO_3H, -COOH, -NH_2, -OH, -CN, -CH_3 and -F groups in MOF-177. Additionally, some researchers have inspected the interaction strength of CO_2 with different functionalized linkers using *ab* initio methods.[32–34] Molecular simulations have been used widely by the researchers to obtain useful information about the adsorption properties of MOFs, even prior to their synthesis.[35–38] Inspired from the above work, we attempted to design various functionalized FMOFs by replacing -CF_3 groups in original structure by X = -OCH_3, -CN, -OH-, -COOH and -NH_2 functional groups. Then we performed a systematic investigation of CO_2, CH_4 and N_2 adsorption behavior of all the MOFs. Henry's constant (K_H) and isosteric heat of adsorption at infinite dilution (Q_{st0}) were obtained by Monte Carlo (MC) simulation, whereas binding energy (BE) was calculated by Möller-Plesset second-order perturbation theory (MP2). Obtained K_H, Q_{st0}, and BE values were used to understand the adsorbate-adsorbent interaction in MOFs. The CO_2 adsorption sites of MOFs were studied by analyzing the radial distribution functions (RDFs) of CO_2 at room temperature. The CO_2/CH_4 and CO_2/N_2 adsorption selectivity were determined by Grand Canonical Monte Carlo (GCMC) simulations in all the functionalized MOF materials. Comprehensively, we inspected the role of the X functional groups on the uptake capacities and selective adsorption of CO_2 over CH_4 and N_2.

2. METHODOLOGIES

2.1 Adsorbent Model

FMOF-1 was considered as the reference adsorbent. This is a fluorous metal organic framework, synthesized by Yang et al.[39] The cell parameters and the coordinates of the framework atoms were taken from the experimental crystallographic data.[40] FMOF-1 has tetragonal crystal

structure with the space group of $I\bar{4}2d$ and the lattice parameters are a = b = 14.0733 Å, c = 37.675 Å, $\alpha = \beta = \gamma = 90^0$. No experimental crystallographic data is available for FMOF-1-X (X = $-OCH_3$, -CN, -OH, -COOH and $-NH_2$). Material Studio was used to construct the hypothetical structures.[41] This program can efficiently generate feasible crystal structures and researchers are using this software to characterize MOF structures prior to their synthesis.[42–44] Considering FMOF-1 as the parent structure, FMOF-1-X were constructed by replacing the $-CF_3$ groups with the X functional groups followed by structure optimization using the Forcite module, implemented in Material Studio program. Universal force field[45] was considered to describe the interactions between the framework atoms during the structure optimization. Final structures (FMOF-1-X) were obtained after finishing the two steps optimization procedure. Energy and density optimization data (Figures S1-S5; see Electronic Supporting Information (ESI)) ensure the reliable hypothetical crystal structures. Rather than having different lattice parameters, all the FMOF-1-X exhibit the same tetragonal crystal structure as the parent FMOF-1, with the space group of $I\bar{4}2d$. The optimized structures of $-OCH_3$, -CN, -OH, -COOH and $-NH_2$ functionalized MOFs along with the parent FMOF-1 are displayed in Figures S6-S8. The structural properties of the MOFs such as density, void fraction and pore volume were computed using Zeo++ software[46] whereas, RASPA2 program[47] was used to determine the accessible surface area considering N_2 as the probe molecule. The geometrical properties of all the MOFs are listed in Table 2 below.

2.2 Interaction Potential

In order to describe the non-bonded interactions during the CO_2, CH_4 and N_2 adsorption in MOFs, we used the interaction potential as a combination of truncated Lennard-Jones (LJ) and Coulomb potential according to Equation (1)

$$V_{ij} = 4\varepsilon_{ij}\left[\left(\frac{\sigma_{ij}}{r_{ij}}\right)^{12} - \left(\frac{\sigma_{ij}}{r_{ij}}\right)^{6}\right] + \frac{q_i q_j}{4\pi\epsilon_0 r_{ij}} \quad (1)$$

-- where the interacting atoms are indicated by *i* and *j*, r_{ij} is their interatomic distance, q_i and q_j are the partial atomic charges of i and j respectively, ε_{ij} and σ_{ij} are the LJ potential parameters describing the well depth and repulsion distance between i and j and ϵ_0 is the dielectric constant. The LJ parameters for the framework atoms were taken from the Universal Force Field (UFF)[45] as tabulated in Table S1. The cross LJ potential parameters were calculated by invoking the Lorentz-Berthelot mixing rules. Appropriate interaction potential parameters and atomic point charges of the framework atoms are crucial for accurate molecular modeling to study the gas adsorption isotherms in MOFs. Since point charges are not obtainable experimentally, so there is no particular charge calculation method that could be used widely for the estimation of the partial atomic charges of framework atoms in MOF structures.[48,49] Consequently, different methods have been developed to date to predict the partial atomic charges of the framework atoms. For instances, the work of Sladekova et al.[49] shows the effect of atomic point charges on adsorption isotherms of CO_2 and H_2O in six MOFs namely IRMOF-1, MIL-47, UiO-66, CuBTC, Co-MOF-74 and SIFSIX-2-Cu-I.

In our work, the atomic partial charges for the -CN, -OH, -COOH and -NH_2 functional groups were adopted from the works of Torrisi et al. and Gu et al.[30,31] while the partial charges of -OCH_3 were estimated by using the density functional theory (DFT) implemented in DMol3 module of Material studio.[41] During the DFT calculation, we used PW91 functional along with the Double-ξ numerical polarization (DNP) basis set. The partial charges of the X-functional groups were derived from the fitting of the energy surface potentials (ESP). ESP charges are being widely used by researchers to study the gas adsorption isotherms for MOF structures,[29–31] as this method generally gives a better description of the electrostatic potential around the different atomic species in MOFs.[30] The partial charges for the rest of the framework atoms were taken from the

work of Moghadam et al.[40] We scaled the charges a little in order to make the frameworks charge neutral. All the framework charges are listed in Table S2-S7. The long-range electrostatic interactions were calculated via the Ewald summation method[50] with the same cutoff distance of 12.8 Å considered for all the Lennard-Jones interactions.

In this study, CO_2 and N_2 molecules were modeled as linear three-site rigid model,[51] whereas CH_4 was mimicked as united spherical single site model.[52] The C-O and N-N bond lengths were 1.16 Å and 1.10 Å, respectively, in CO_2 and N_2. The charges on C and O atoms were +0.70 e and -0.35 e in CO_2. On the other hand, a charge of -0.482 e and +0.964 e was placed on N and on center-of-mass respectively during the modeling of N_2. These partial charges on the LJ sites were used to describe the internal quadrupole moment of CO_2 and N_2. We used the transferable potentials for phase equilibria (TraPPE) force field to model the adsorbates (CO_2, CH_4 and N_2). The potential parameters and the atomic charges of the adsorbates are listed in Table S8. A 2 × 2 × 1 supercell was used for all MOF structures. The framework atoms were kept rigid during GCMC simulations.

2.3 Simulation Details

Simulation studies have disclosed that Grand Canonical Monte Carlo (GCMC) simulations can accurately compute the gas loading in porous materials such as in MOFs.[53] We used GCMC to calculate the pure CO_2, CH_4, N_2 and binary mixtures of CO_2/CH_4 & CO_2/N_2 adsorption isotherms as a function of pressure. The calculations were carried out at 273 K and 298 K up to a pressure of 30 bar in all the structures. The number of gas molecules in the adsorbed phase was allowed to fluctuate whereas the chemical potential (μ), volume (v), and temperature (T) were kept constant during the GCMC simulations. Random insertion, deletion, rotation and translation with equal probabilities were used in each MC run. The GCMC calculation at each pressure point was consisted of 2.0×10^5 number of cycles. The first half was used for equilibration and the subsequent

half was used to estimate the desired adsorption properties. Excess adsorption isotherms were simulated by considering the void fraction of both structures (details can be found in SI).

The Henry's constants (K_H) of the adsorbates were evaluated using the Widom particle insertion method.[54] The enthalpy of adsorption, ΔH was determined by the statistical average of the adsorbate binding energies at different available adsorbent sites according to Equation (2)

$$\Delta H = \frac{\langle U \times N \rangle_\mu - \langle U \rangle_\mu \langle N \rangle_\mu}{\langle N^2 \rangle_\mu - \langle N \rangle_\mu^2} - \langle U_g \rangle - RT \qquad (2)$$

-- where, N is the number of adsorbed molecules, R is the universal gas constant, and ⟨ ⟩ defines the ensemble average.

The isosteric heat of adsorption at infinite dilution, Q_{st0} was estimated using a single molecule of the adsorbates in Canonical ensemble (*NVT*), as the following Equation,

$$Q_{St0} = -\Delta H = \langle U_{hg} \rangle - \langle U_h \rangle - \langle U_g \rangle - RT \qquad (3)$$

-- where $\langle U_{hg} \rangle$, $\langle U_h \rangle$ and $\langle U_g \rangle$ are the average energy of the single guest molecule inside the host, the average energy of the host, the average energy of a single guest molecule in the gas phase. The isosteric heat of adsorption at finite dilution, *Qst* was computed using the fluctuation method,[55] implemented in the RASPA2 software package.[47] The *Qst* values were predicted from the fluctuations of the potential energy over the production cycles in the GCMC simulations for each pressure point.

To break down the relative contributions of van der Waals and Coulombic interactions to the interaction energy between MOF and adsorbate molecules, we performed energy minimizations of a single adsorbate molecule inside the MOF structures employing (NVT) ensemble. From this force field-based molecular simulations, the minimum host-adsorbate energy was obtained via

Baker's method[56] and used for further analysis of the van der Waals and Coulombic contributions to the interaction energy. Baker's minimization[56] for 100 independent minimization attempts with the stopping criteria of RMS gradient of 1.0×10^{-6} was also considered to find the favorable adsorption sites of the adsorbates (CO_2, CH_4 and N_2). During Baker's minimization, framework atoms were held fixed, whereas a single molecule of the adsorbate gases were relaxed within the rigid MOF structures. Two types of trial moves, namely translation and rotation with equal probability were attempted for the adsorbate molecules. In the Baker's minimization method, the equilibrium geometrics of the adsorbate molecules were estimated from the force field-based molecular simulations. All simulations, such as GCMC, Widom particle insertion calculations, and energy minimizations (via Baker's method), were carried out using the RASPA2 software package.[47] The binding energy (BE) of CO_2 molecule with the various functional groups of the frameworks was computed by Möller-Plesset second-order perturbation theory (MP2) with Def2TZVP basis set. These calculations were performed using the Gaussian 16 code.[57] Further computational details can be found in Section 3.4.

We also simulated the adsorption isotherms considering the bulk composition of 50:50 in CO_2/CH_4 and 15:85 in CO_2/N_2 binary mixtures. These compositions of the binary systems represent the landfill gas separation and flue gas separation, respectively.[58] The ideal adsorbed solution theory (IAST)[59] was invoked to predict the adsorption selectivity of CO_2/CH_4 and CO_2/N_2 binary mixture from their pure component adsorption isotherms. The selectivities were predicted at the above-mentioned composition at 298 K with a pressure range up to 0-1 bar.

All the structures were assessed in view of the three adsorbent evaluation criteria for their CO_2 separation capability over CH_4 and N_2. The adsorbent evaluation criteria are: 1) CO_2 uptake under

adsorption conditions (mol/kg), N^{ads}; 2) working capacity of CO_2 (mol/kg), $\Delta N = N^{ads} - N^{des}$, and 3) selectivity, $S = (N_{CO2}^{ads} / N_W^{ads})(y_W / y_{CO2})$. Here, N is the adsorbed amount, y is the gas phase mol fraction, W indicates the weakly adsorbed gas component (CH_4 or N_2), and superscripts *ads* and *des* are the adsorption and desorption conditions, respectively. We measured these parameters for three cases as listed in Table 1 and ranked all the functional FMOFs based on their selectivity.

Table 1: Binary mixture proportions and pressures for the cases studies in this work

Cases	Mixture proportion	Adsorption pressure, P^{ads} (bar)	Desorption pressure, P^{des} (bar)
Natural gas purification	CO_2/CH_4 = 10:90	5	1
Landfill gas separation	CO_2/CH_4 = 50:50	1	0.1
Flue gas separation	CO_2/N_2 = 15:85	1	0.1

The CO_2, CH_4 and N_2 uptake were estimated at the partial pressure of the specific gas component under the adsorption and desorption conditions.

To confirm the reliability of the forcefield used in this study, we first simulated N_2 adsorption in FMOF-1 at 77 K and compared it with the previous simulated data.[40] We observe the similar trend of N_2 adsorption but a lower uptake compared the previous simulated data. The slight variation of N_2 loading could be due to the different void fractions used during simulations. However, the forcefield is validated by the identical shape of the isotherms depicted in Figure S9.

3. RESULTS AND DISCUSSION

Table 2. Geometric properties for the MOF structures studied in this work.

Structure	Density (g/cm^3)	Pore Volume (cm^3/g)	He Void Fraction	Surface Area (m^2/g)
FMOF-1	1.666	0.248	0.413	826.537
FMOF-1-OCH_3	1.323	0.348	0.461	1215.416
FMOF-1-CN	1.330	0.332	0.442	1168.435
FMOF-1-OH	1.264	0.456	0.576	1492.484
FMOF-1-COOH	1.676	0.217	0.364	704.115
FMOF-1-NH_2	1.215	0.472	0.573	1523.289

From the geometric properties of the structures listed in Table 2, we observe increased surface areas and pore volumes of -OCH_3, -CN, -OH and -NH_2 functionalized MOFs compared to the parent FMOF-1 structure, while we notice a decreasing trend for the density. In contrast with the other functionalized MOFs, we observe decreased surface area and pore volume for the -COOH functionalized MOF, compared with the parent FMOF-1. Likewise, higher density of the -COOH functionalized MOF was found. We speculate this opposite trend for the -COOH functionalized MOF is due to the size of the bulky -COOH group compared to the other functional groups. The pore size distribution (PSD) of the MOFs are shown in Figure 1. The channel diameter has increased to 6.93 Å in FMOF-1-CN, 6.99 Å in FMOF-1-OH, and 6.63 Å in FMOF-1-NH_2 from 6.40 Å in the parent structure. On the other hand, channel diameter has decreased to 5.55 Å and 5.31 Å, respectively, in FMOF-1-OCH_3 and FMOF-1-COOH.

N_2 adsorption isotherms at 77 K for all the functionalized MOFs are depicted in Figure S10. All the studied MOFs display type I adsorption profile, exhibiting characteristic microporous behavior.

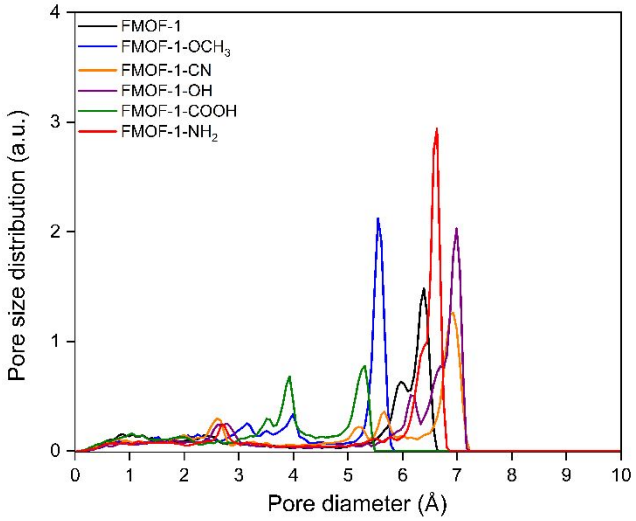

Figure 1. Pore size distributions of the MOF structures.

3.1 Energy parameters at infinite dilution

Henry's constant, K_H and isosteric heat of adsorption at infinite dilution, Q_{st0} can reflect the adsorbate-adsorbent interaction strength in the Henry regime. The larger K_H and, Q_{st0} values represent the greater adsorbate affinity to the adsorbent.[60] K_H and Q_{st0} values for CO_2, CH_4, and N_2 at 273 K and 298 K were predicted from GCMC simulation and the results at 298 K are listed in Tables 3 and 4, respectively. The values at 273 K are tabulated in Tables S9 and S10.

Table 3. Henry's constant, K_H at 298 K.

Structure	Henry constant, K_H (mol/kg/Pa)		
	CO_2	CH_4	N_2
FMOF-1	1.81×10^{-6}	1.23×10^{-6}	4.95×10^{-7}
FMOF-1-OCH_3	4.10×10^{-6}	2.12×10^{-6}	7.55×10^{-7}
FMOF-1-CN	5.11×10^{-6}	1.34×10^{-6}	6.14×10^{-7}
FMOF-1-OH	3.64×10^{-5}	1.32×10^{-6}	7.90×10^{-7}
FMOF-1-COOH	1.02×10^{-4}	2.04×10^{-6}	9.62×10^{-7}
FMOF-1-NH_2	7.01×10^{-5}	2.08×10^{-6}	1.09×10^{-6}

Table 4. Isosteric heat of adsorption at infinite dilution, Q_{st0} at 298 K.

Structure	Isosteric heat of adsorption at infinite dilution, Q_{st0} (kJ/mol)		
	CO_2	CH_4	N_2
FMOF-1	-13.67	-11.40	-9.01
FMOF-1-OCH_3	-16.94	-13.18	-10.35
FMOF-1-CN	-17.75	-11.63	-9.56
FMOF-1-OH	-29.33	-10.44	-9.63
FMOF-1-COOH	-31.04	-15.47	-14.36
FMOF-1-NH_2	-31.37	-11.62	-10.75

The order of K_H and Q_{st0} was found as is $CO_2 > CH_4 > N_2$ for all the MOFs, implying the stronger CO_2-framework interactions compared to CH_4-framework and N_2-framework interactions. This phenomenon might be due to the larger permanent quadrupole moment of the CO_2 molecule.[61] According to the simulation, an increased K_H and Q_{st0} (except for the Q_{st0} of CH_4 in -OH functionalized structure) values were noticed for all the X-functionalized MOFs compared to the parent MOF for all the adsorbates. Notably, -OH, -COOH and -NH_2 groups have displayed significant improvement for the K_H and Q_{st0} values for CO_2. These enhanced values of the parameters could be described by the stronger polarity of the -OH, -COOH and -NH_2 groups compared to other functional groups. This assumption could be further supported by the results of the relative contribution of van der Waals (vdW) and coulombic interactions to the total interaction energy of CO_2 in the studied MOFs, that has been discussed in section 3.3. The larger K_H and Q_{st0} values of CO_2, CH_4, and N_2 in all the X-functionalized MOFs compared to the parent MOF exhibit greater affinity and stronger interaction strength to the frameworks.

3.2 Pure gas adsorption isotherms

We simulated the adsorption isotherms of pure component CO_2, CH_4 and N_2 in all the X-functionalized MOFs along with the parent FMOF at 273 and 298 K with a pressure range up to 30 bar. Figure 2 shows the CO_2 uptake for all the MOF structures at 298 K in low-pressure (0.005-1 bar) as well as high-pressure (1-30 bar) region. An enhanced CO_2 uptake was observed for the X-functionalized MOFs compared to the parent MOF. The order of CO_2 uptake up to 0.2 bar (Figure 2a) is FMOF-1-COOH > FMOF-1-NH_2 > FMOF-1-OH > FMOF-1-CN > FMOF-1-OCH_3 > FMOF-1. This is consistent with the order of the predicted Henry's constant (K_H values in Table 2). With the increase in pressure, a different CO_2 adsorption profile was observed for the studied MOFs. At low pressure region, gas adsorption is generally dominated by the host-guest interaction,[62] as reflected in the Henry's constant values. In contrast, at high pressure region the adsorption capacity primarily depends on the available free volume of the framework structure.[62] As shown in Figure 2, -COOH functionalized MOF exhibits the highest CO_2 uptake below 0.2 bar, while at 30 bar a comparable CO_2 uptake was predicted for FMOF-1-COOH and FMOF-1. This comparable CO_2 uptake is due to the similar free volumes and surface areas of the structures (Table 1). At 1 bar pressure, the -OH and -NH_2 functionalized structures show the maximum CO_2 uptake with a value of □3.0 mol/kg. This value is about 15-fold higher than that of the parent FMOF-1 (□0.2 mol/kg) and 1.5-fold higher than the IRMOF-1 (2.1 mmol/g at 295 K)[63]; but lower than the zeolite NaX and NaY structures (□4.5 mol/kg at 298 K)[64,65] at 1 bar. We also observe higher CO_2 uptake for all the X-functionalized MOFs compared to the parent MOF at high-pressure region. The highest CO_2 uptake was observed for FMOF-1-OH with a value of 10.07 mol/kg at 30 bar at 298 K, which is 3.35-fold higher than the parent FMOF-1 with the value of 2.85 mol/kg. A similar trend was observed for CO_2 adsorption isotherms at 273 K, shown in Figure S11.

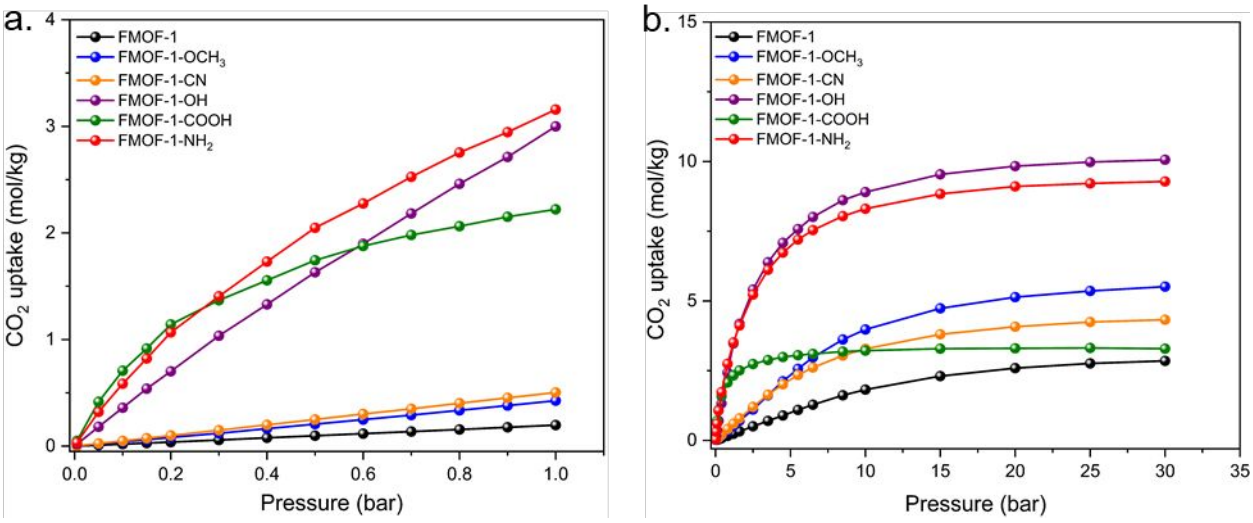

Figure 2. CO_2 adsorption isotherms at (a) low pressure and (b) high pressure regions of MOFs at 298 K.

Pure component CH_4 and N_2 adsorption isotherms at 298 K are depicted in Figure 3 and Figure 4 respectively, whereas Figures S12 and S13 show the isotherms at 273 K. At low pressure region (Figure 3a), the order of CH_4 uptake is FMOF-1-OCH_3 > FMOF-1-NH_2 > FMOF-1-COOH > FMOF-1-CN > FMOF-1-OH > FMOF-1. For N_2 adsorption the order was found as FMOF-1-NH_2 > FMOF-1-COOH > FMOF-1-OCH_3 > FMOF-1-OH > FMOF-1-CN > FMOF-1 (Figure 4a). These orders of CH_4 and N_2 uptake are consistent with the orders of predicted Henry's constant (K_H values in Table 3). At high pressure region, a different order of CH_4 and N_2 adsorption was observed for the studied MOFs.

We observe the rise of CO_2 uptake in a different scale than that of the rise of CH_4 and N_2 uptake with the increase in pressure up to 30 bar. The CO_2 adsorption isotherms exhibit a sharp rise at low pressure region compared to CH_4 and N_2 adsorption and then reaches a plateau at around 20 bar. On the other hand, CH_4 and N_2 isotherms do not show a steep uptake in low-pressure region. This expected finding is consistent with the relatively smaller Q_{st0} values of CH_4 and N_2 compared to the Q_{st0} value of CO_2 (Table 3). CH_4 and N_2 uptake increase gradually with the pressure and do

not saturate, even at the highest pressure at 30 bar. The maximum CH_4 uptake at 1 bar was observed for FMOF-1-OCH_3 (0.19 mol/kg) which is 1.8 times higher than that of the parent FMOF-1 (0.11 mol/kg). FMOF-1-NH_2 shows the maximum N_2 uptake with a value of 0.09 mol/kg which is 2.3 times higher compared to FMOF-1 (0.04 mol/kg) at the same condition (1 bar and 298 K).

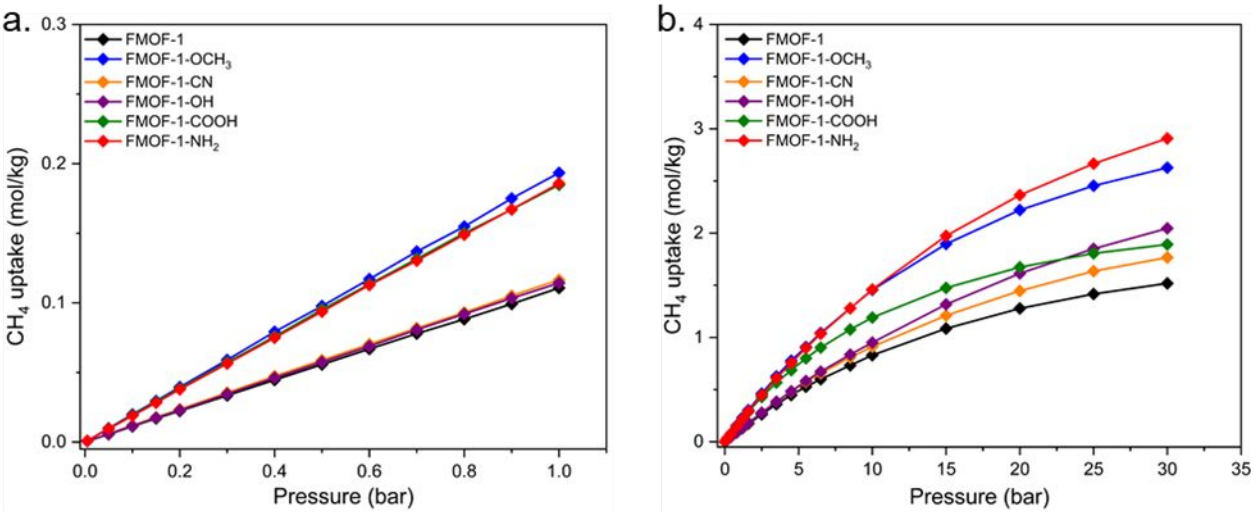

Figure 3. CH_4 adsorption isotherms at (a) low pressure and (b) high pressure regions of MOFs at 298 K.

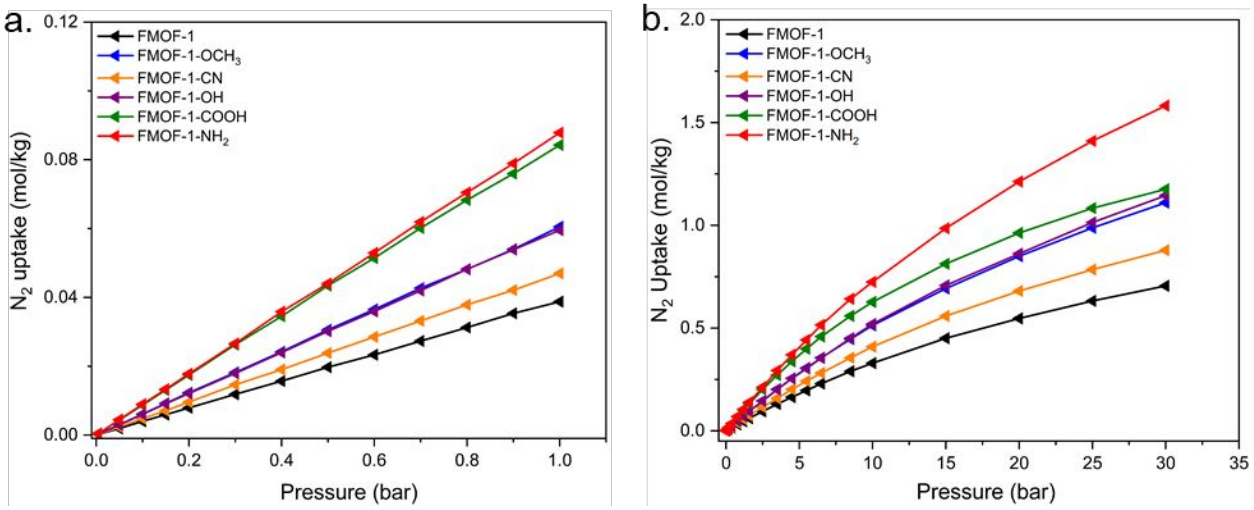

Figure 4. N_2 adsorption isotherms at (a) low pressure and (b) high pressure regions of MOFs at 298 K.

3.3 Isosteric heats of adsorption, Q_{st}

The isosteric heats of adsorption (Q_{st}) for CO_2, CH_4 and N_2 were obtained by the GCMC simulations during the adsorption isotherm calculations. Figure 5 and Figure S14 displays the Q_{st}

values as a function of pressure and uptake, respectively, at 298 K. It is observed that, for all the MOF structures, the Q_{st} values of CO_2 are higher compared to the values obtained for CH_4 and N_2. Consequently, the order of isosteric heat of adsorption is $CO_2 > CH_4 > N_2$ for all the structures, consistent with the order of the uptake capacity. At 0.005 bar, the isosteric heats of adsorption of CO_2 were estimated as 16.92, 17.70, 29.42, 30.98, and 31.07 kJ/mol, respectively, for -OCH_3, -CN, -OH, -COOH and -NH_2 functionalized MOFs. All these Q_{st} values are higher compared to the Q_{st} value of CO_2 for the parent FMOF-1 (13.65 kJ/mol). The larger CO_2 Q_{st} values for the X-functionalized MOFs than that of the parent MOF over the entire pressure range demonstrates the more energetic CO_2 interaction with the X-functionalized MOFs. The CO_2 Q_{st} for FMOF-1-OH and FMOF-1-NH_2 first declines to 29.24 and 28.15 kJ/mol, respectively, at around 5 bar (Figure 5a) due to the adsorbate-adsorbent interaction, i.e., the interactions of the CO_2 quadrupole with the most active adsorption centers of the adsorbents play the dominant role in this region. Subsequently, we notice an increasing trend of CO_2 Q_{st} with the increase in uptake or pressure, because of the increased CO_2-CO_2 interactions. For FMOF-1-COOH, the CO_2 Q_{st} first increases up to 5 bar, reaches to a value of 32.23 kJ/mol and then decreases with the increase in pressure or CO_2 loadings. For FMOF-1-OH, FMOF-1-COOH and FMOF-1-NH_2, the presence of different energetic CO_2 adsorption sites, i.e., the surface heterogeneity[30] results in the maxima and minima of the Q_{st} of CO_2 curves for these structures. For the other functionalized MOFs including the parent MOF, the relationship of Q_{st} vs pressure (Figure 5a) or Q_{st} vs CO_2 uptake (Figure S14a) is similar. The CO_2 Q_{st} increases evenly to a value of 27.69, 25.11 and 21.93 kJ/mol for FMOF-1-OCH_3, FMOF-1-CN and FMOF-1, respectively, up to 30 bar. The increasing behavior is due to the lateral interactions of the guest molecules with the increase in pressure (or the adsorbate concentration).[66,67]

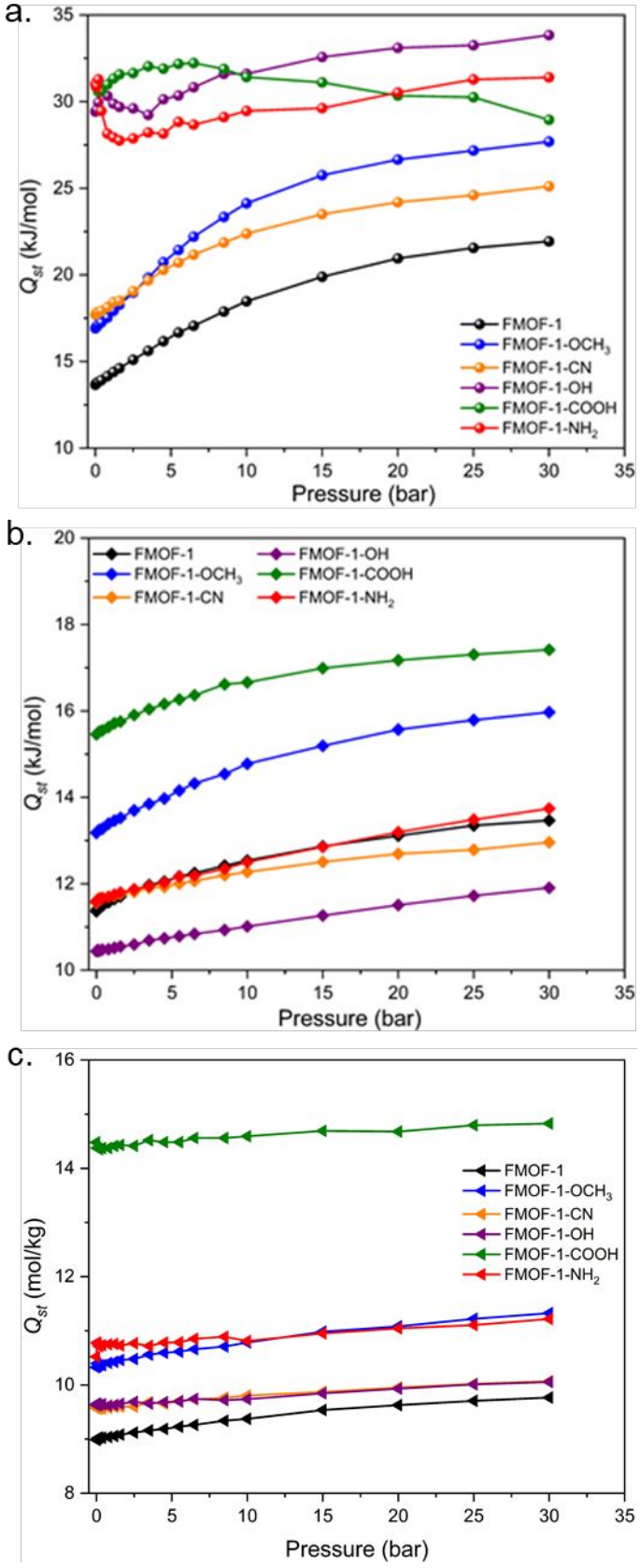

Figure 5. GCMC simulated isosteric heats of adsorption for (a) CO_2, (b) CH_4, and (c) N_2 at 298 K up to 30 bar.

Figure 5b and 5c depicts the Q_{st} of CH_4 and N_2, respectively, at 298 K. For CH_4, we observe a moderate variation in Q_{st} with the increase in pressure or CH_4 loading. The increase of CH_4 Q_{st} values were found as 11.36 to 13.47 kJ/mol for FMOF-1, 13.18 to 15.97 kJ/mol for FMOF-1-OCH_3, 11.56 to 12.96 kJ/mol for FMOF-1-CN, 10.43 to 11.90 kJ/mol for FMOF-1-OH, 15.46 to 17.42 kJ/mol for FMOF-1-COOH, and 11.58 to 13.74 kJ/mol for FMOF-1-NH_2. For FMOF-1-OH, we notice lower Q_{st} values through the entire pressure range compared to the parent MOF. This might be due to the larger void fraction of -OH functionalized structure compared to the parent structure (Table 1) and the relatively smaller CH_4 K_H value (Table 2). On the other hand, FMOF-1-CN shows a decreasing trend of Q_{st} values compared to the parent MOF beyond 2.5 bar. This could be attributed to the similar K_H values of CH_4 in FMOF-1-OH and FMOF-1-CN as well as the comparable void fraction of FMOF-1-OH with FMOF-1 (0.442 vs 0.413).

Unlike the Q_{st} values of CO_2 and CH_4, the Q_{st} of N_2 remains almost constant through the entire pressure range. This outcome indicates the relatively weaker interaction of the CH_4 and N_2 molecules with the MOF structures compared to the CO_2-MOF interactions.

It is relevant to note that an enhanced CO_2, CH_4 and N_2 adsorption was observed for all the X-functionalized MOFs compared to the parent MOF, but the Q_{st} orders of CO_2, CH_4 and N_2 in those structures did not follow the same trend. This is because Q_{st} is not the only factor that reflects the adsorption isotherm, rather it is one of many factors that affect the adsorption capacity and could reflect the adsorption amount to a certain extent.[60] The Q_{st} values at 273 K are depicted in Figures S15-S17.

From the relative contribution of van der Waals (vdW) and coulombic interactions to the total interaction energy of CO_2, CH_4 and N_2 in the studied MOFs (Figure 6) it is apparent that, the

significantly improved CO_2 adsorption capacity in -OH, -COOH and -NH_2 functionalized structures is due to the enhanced coulombic interaction compared to the parent FMOF-1. On the other hand, for N_2-MOF interaction energy, the vdW interactions play the dominant role with a little coulombic contribution for those structures. In contrast, the interaction energy for CH_4 was purely from the van der Waals interactions without any electrostatic contribution. This could be due to the larger quadrupole moment of CO_2 (4.30×10^{-26} esu-cm^2) compared to the smaller quadrupole moment of N_2 (1.52×10^{-26} esu-cm^2) and zero-quadrupole moment of CH_4.[61]

We performed additional simulations by omitting the coulombic interaction of the guest molecules with the framework atoms to investigate the effect of electrostatic interactions on CO_2, CH_4 and N_2 adsorption at 298 K up to 1 bar (Figures 7 and S18-19). Disregarding the electrostatic interaction, a lower CO_2 and N_2 uptake were observed for all the MOF structures. In contrast, CH_4 uptake was not influenced by turning off the coulombic interaction. We observe a larger variation of CO_2 uptake while we consider the coulombic interaction than that of the uptake without considering the coulombic interaction. For N_2 uptake, the variation was not as prominent as CO_2. This finding is quite consistent with the results discussed above and demonstrates the importance of electrostatic interactions on enhanced CO_2 adsorption in -OH, -COOH and -NH_2 functionalized structures.

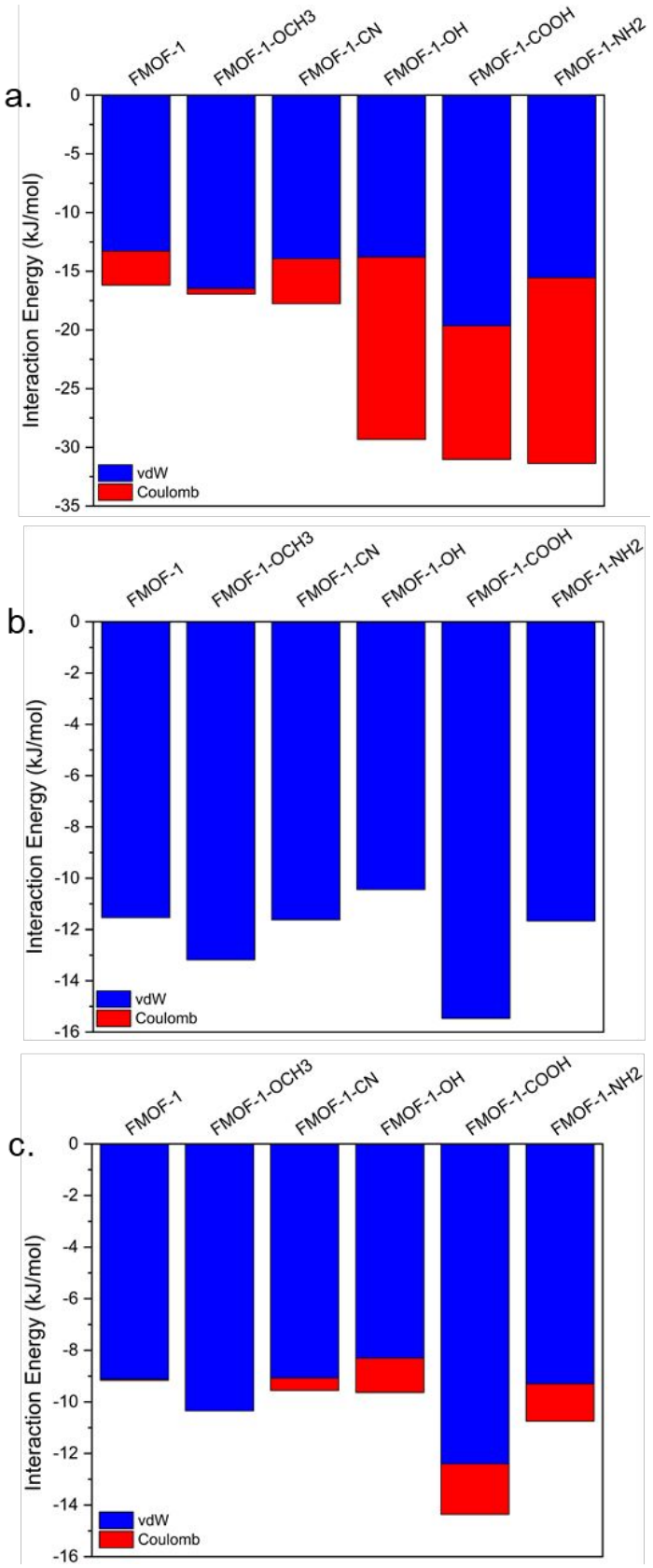

Figure 6. Interaction energy plot for (a) CO_2, (b) CH_4, and (c) N_2 in the investigated MOFs.

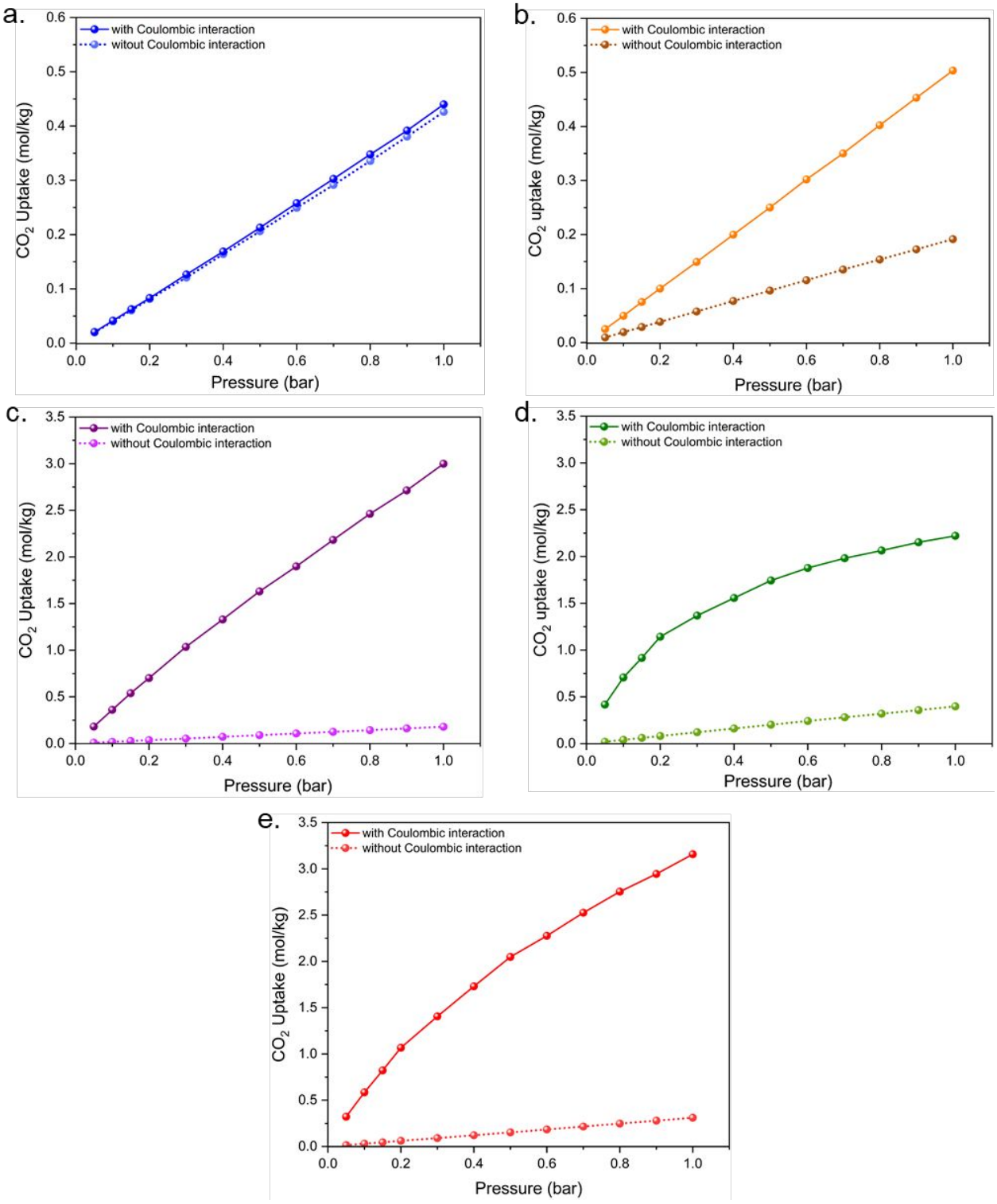

Figure 7. Comparison of CO_2 adsorption isotherms obtained by considering or neglecting electrostatic interactions in (a) FMOF-1-OCH_3, (b) FMOF-1-CN, (c) FMOF-1-OH, (d) FMOF-1-COOH, and (e) FMOF-1-NH_2 at 298 K.

3.4 Interaction of CO_2 with the functional groups of the framework

The binding energy (BE) of CO_2 with various functional groups of the framework was computed by Möller-Plesset second-order perturbation theory (MP2) with triple-ξ valence basis set with polarization (Def2TZVP).[68] The rationale for the selection of Def2TZVP basis set is that it can efficiently capture the dispersion interaction.[6,34,69] For BE calculation between CO_2 and X-functional groups using MP2, a small model of triazole ring containing two -CF_3 or two X-substituents (in the 3,5-positions) was constructed (Figure 8). Only a small model was constructed to reduce computational cost. All the models (the triazole ring containing the -CF_3 or X-substituents in the 3,5-positions) were optimized first using MP2/ Def2TZVP level of theory. Then geometry optimization was done for the CO_2-triazole complex considering different geometrics (positions and orientations) of CO_2 around the functional groups. Eventually, the BE of CO_2 around different functional groups was calculated as per the following Equation:

$$BE = E_{CO_2-triazole\ model} - (E_{CO_2} + E_{triazole\ model}) \qquad (4)$$

--where, $E_{CO_2}$is the energy of CO_2, $E_{trizole\ model}$ is the energy of the small triazole model, and $E_{CO_2-trizole\ model}$ is the energy of CO_2-trizole complex under equilibrium state. Figure 8 shows the most stable complexes.

As per the optimized structures, the electropositive C atom of CO_2 interacts with the electronegative N and O atoms of -CN and -COOH functional groups, while hydrogen bonding interactions were observed for -OCH_3, -NH_2 and -OH functional groups with a distance of □3.50, 2.60 and 2.13 Å, respectively. The highest binding energy value was observed for the -NH_2-CO_2 structure (-21.09 kJ/mol) followed by the -OH-CO_2 structure (-18.10 kJ/mol). Although the O(CO_2)---H(-OH) distance exhibits a relatively smaller value (2.13 Å) than that of the average

O(CO_2)---H(-NH_2) distance (2.60 Å), the multiple interaction between the terminal O atoms of CO_2 with the H atoms of NH_2 results in increased binding energy for the NH_2-CO_2 structure. For the -COOH-CO_2 structure, we notice the CO_2 molecule is tilted towards the $O_{carbonyl}$ of -COOH group with a distance of 3.00 Å and a binding energy of -17.97 kJ/mol. We do not observe any hydrogen bonding interaction for the -COOH-CO_2 structure, as the H(-COOH) atom is pointing away from the CO_2 molecule in the optimized configuration. The -OCH_3-CO_2 structure shows the least BE value (-10.22 kJ/mol) among all the structures.

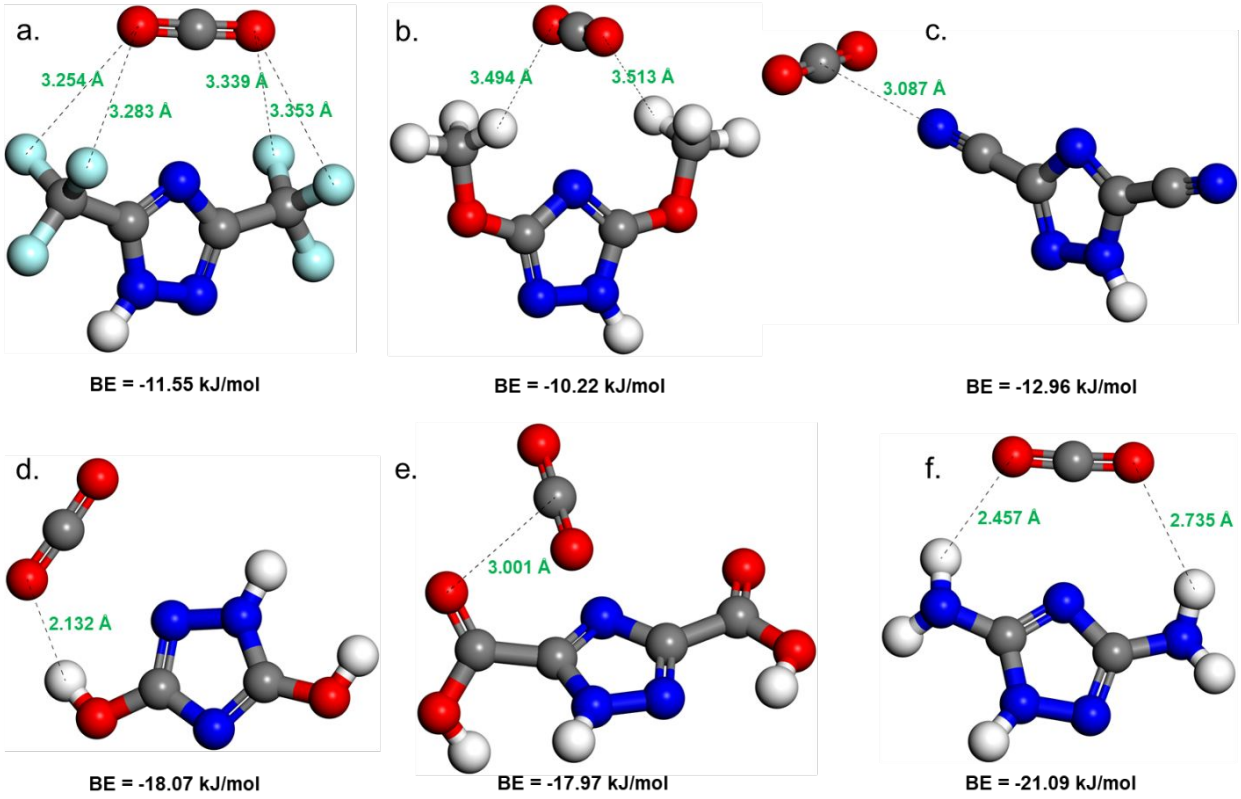

Figure 8. Optimized structures and interaction energies of CO_2 with (a) −CF_3, (b) −OCH_3, (c) −CN, (d) −OH, (e) −COOH, and (f) −NH_2 functional groups of MOFs. Color code (C: gray, O: red, N: blue, H: white and F: cyan).

The binding energies (BE) of CO_2 with different functional groups calculated by MP2 level of theory follow the order of FMOF-1-OCH_3 < FMOF-1 < FMOF-1-CN < FMOF-1-COOH < FMOF-1-OH < FMOF-1-NH_2 (Figure 8). This order shows a slight disagreement from the isosteric heat

of adsorption at infinite dilution, Q_{st0} for CO_2 predicted from force-field based molecular simulation, that follow the order of FMOF-1 < FMOF-1-OCH_3 < FMOF-1-CN < FMOF-1-OH < FMOF-1-COOH < FMOF-1-NH_2 (Table 4). More precisely we observe the disagreement between FMOF-1 and FMOF-1-OCH_3 and between FMOF-1-COOH and FMOF-1-OH.

For the calculations obtained by MP2 we observe a large number of interactions between the CO_2 molecule and the F atoms (of -CF_3 groups) in FMOF-1, compared to the number of interactions between the CO_2 molecule and the H atoms (of -CH_3 groups) in FMOF-1-OCH_3. This results in an increased binding energy for the former. On the other hand, the smaller distance between O(CO_2)---H(-OH) (2.132 Å) compared to the distance between C(CO_2)---$O_{carbonyl}$ (-COOH) (3.001 Å) results in a slight increase in binding energy value for FMOF-1-OH. This disagreement for the order of Q_{st0} and BE values obtained by force-field based molecular simulation and MP2/DFT calculations has also been reported by other researchers.[6,31] However, we notice a significant enhancement of the Q_{st0} and BE values for -COOH, -OH and -NH_2 functionalized structures than that of the parent FMOF-1 structure, using both the force-field based molecular simulation and MP2 calculations.

The radial distribution functions (RDF), g(r) between CO_2 and various functional groups of the studied MOFs at 298 K and 0.1 bar are being displayed in Figure 9. For the parent FMOF-1, the g(r) of O(CO_2) around F(-CF_3) is essentially zero with a distance, r < 2.50 Å and exhibits a lower peak at 6.38 Å. On the other hand, a pronounced peak between O(CO_2) and H(-OCH_3) was observed at a distance between 3.42 to 3.78 Å for FMOF-1-OCH_3, whereas a sharp peak between C(CO_2) and N(-CN) was found at r = 3.54 Å for FMOF-1-CN. Unlike the other MOFs, FMOF-1-OH, FMOF-1-COOH and FMOF-1-NH_2 exhibit multiple peaks in g(r) curves. The g(r) between the O(CO_2) and H(-OH) for FMOF-1-OH shows two distinct peaks at 2.94 and 7.54 Å. For FMOF-

1-COOH, we observe three dominant peaks between C(CO_2) and $O_{carbonyl}$ (-COOH) at nearly 3.00, 7.89, and 9.42 Å. Likewise three major peaks between C(CO_2) and H(-NH_2) were found at nearly 2.66, 6.58, and 8.43 Å for FMOF-1-NH_2. The presence of multiple peaks in the g(r) curves suggests multiple CO_2 interactions with neighboring ligands' X substituents in FMOF alternatives.[6] This structural analysis reveals that, CO_2 molecules are preferentially adsorbed towards X groups but at different distances, depending on the interaction strengths of CO_2 with the new MOF structure.

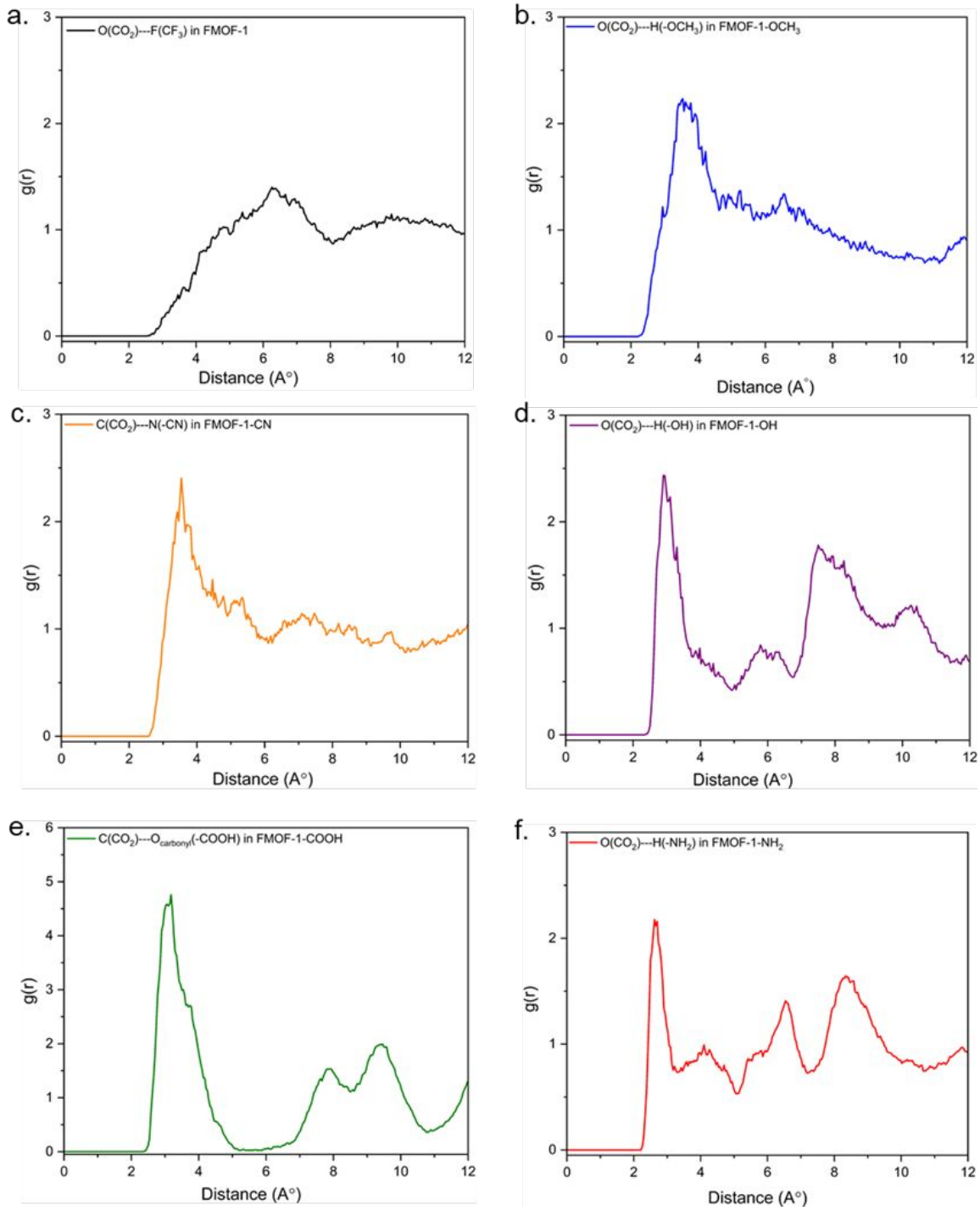

Figure 9. Radial distribution functions for CO_2 near different functional groups of (a) FMOF-1, (b) FMOF-1-OCH_3, (c) FMOF-1-CN, (d) FMOF-1-OH, (e) FMOF-1-COOH, and (f) FMOF-1-NH_2 at 0.1 bar.

We also performed the Baker's minimization by inserting a single adsorbate molecule in the X-functionalized MOFs at 298 K in order to locate the favorable adsorption sites of the adsorbates.

Baker's algorithm[56] uses the eigenvalues of the Hessian matrix in order to locate true minima on the energy surface that corresponds to the equilibrium geometries. The positions of CO_2 (Figure 10) and CH_4 & N_2 (Figure S20) represent the preferred binding sites of the adsorbates in MOFs, predicted by Monte Carlo (MC) simulation.

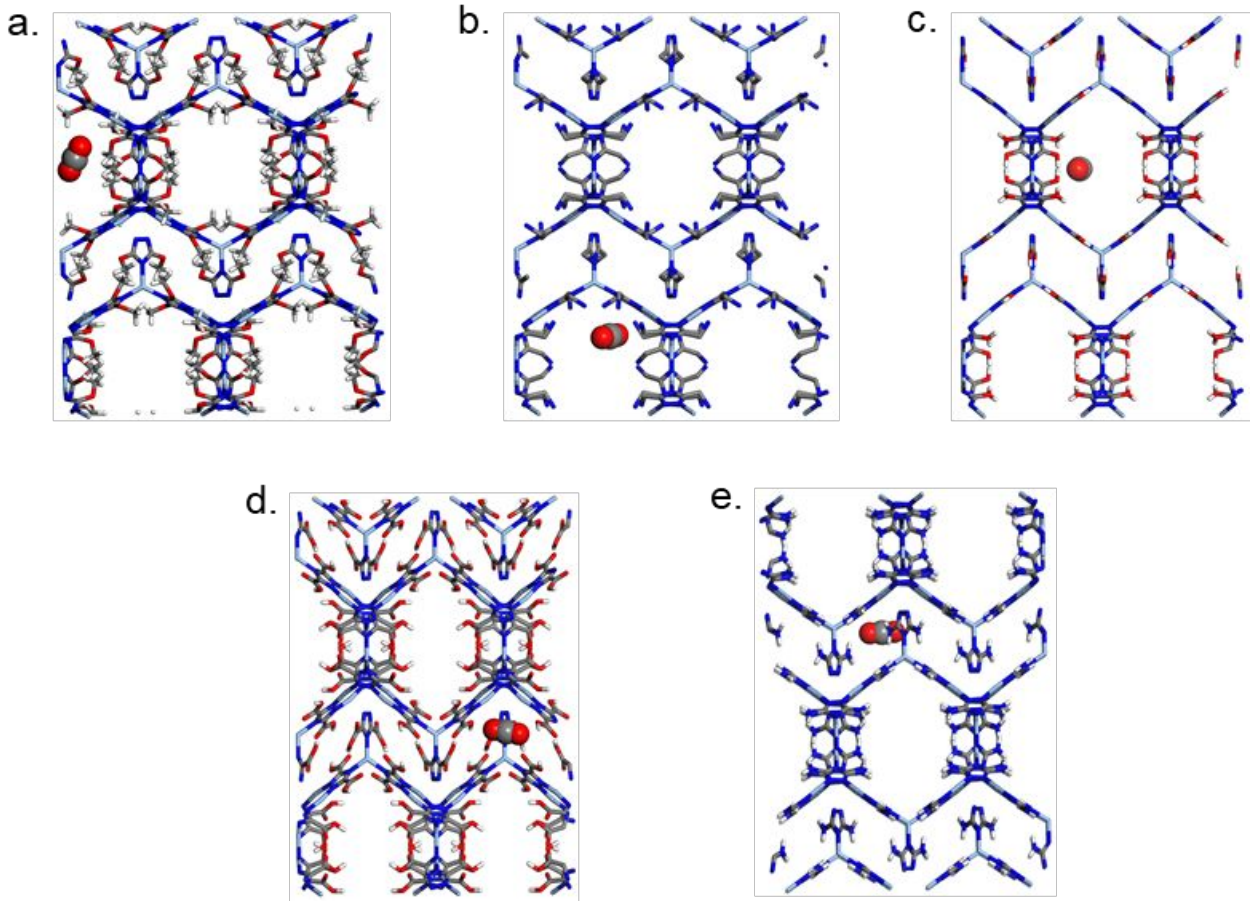

Figure 10. Adsorption sites of CO_2 in (a) -OCH_3, (b) -CN, (c) -OH, (d) -COOH, and (e) -NH_2 functionalized MOFs after Baker's minimization.

We also compared the equilibrium geometrics of the adsorbate molecules after Baker's minimization, estimated from the force field-based molecular simulations with the MP2 calculations. In MP2 calculation, we investigated the probable adsorption sites of CO_2 by studying their dispersion interaction energies using a small model. Only the triazole ring containing two -CF_3 or two X-substituents in the 3,5- positions was used during the molecular model for the study

of interaction energy of CO_2 (Figure 8). As per the MP2 calculation, CO_2 molecules seem to interact with the -CF_3 group for parent FMOF-1 and -X functional groups for X-functionalized MOF structures.

On the other hand, the equilibrium geometrics of CO_2 molecules after Baker's minimization estimated from the force field-based molecular simulations are shown in Figure 10. According to Figure 10, CO_2 molecules are preferentially adsorbed towards -X functional groups rather than the metal cluster sites. This finding is fairly consistent with the adsorption sites calculated from MP2. Still there is a slight discrepancy between the binding distances of CO_2 with -X functional groups, computed from force field-based molecular simulations and MP2 model. For example, the distances between O(CO_2)---H(-OCH_3) in FMOF-1-OCH_3 were 3.503 and 3.601 Å, respectively, obtained from MP2 model and force field-based molecular simulations. This little variation could be qualitatively explained by comparing the two models. In MP2 model, we considered a small segment of the framework, where the influence of neighboring linkers on CO_2 adsorption had been ignored. In contrast, we considered the entire framework during the force field-based molecular simulations (Baker's minimization) to predict the CO_2 adsorption sites, accounting the influence of neighboring linkers on CO_2 adsorption.

3.5 Adsorption of binary mixture and selectivity

We simulated the adsorption isotherms of CO_2/CH_4 and CO_2/N_2 gas mixtures with the composition of 50:50 and 15:85 mole ratio, respectively, to study the carbon capture capability from the landfill and flue gases. Figure 11 shows the adsorption isotherms of the binary mixtures for all the MOFs at 298 K up to a pressure of 1 bar. CO_2, CH_4 and N_2 adsorption exhibit a nearly linear isotherm with the increasing pressure except for the CO_2 adsorption in -COOH functionalized MOF. We

assume this non-linearity is due to the relatively higher pore volume of the other structures than that of the FMOF-1-COOH structure. We also notice preferential adsorption of CO_2 over CH_4 in all the MOFs for the CO_2/CH_4 mixture. Higher CO_2 uptake was observed for the X-functionalized MOFs compared to the parent FMOF-1 structure. Especially for FMOF-1-NH_2, dominant CO_2 uptake was observed over CH_4 due to the enhanced electrostatic interaction in addition to the dispersion interactions. In case of CO_2/N_2 gas mixture, the parent FMOF-1 displays higher N_2 uptake over CO_2 throughout the entire pressure range due to the higher mole fraction of N_2 in the CO_2/N_2 binary mixture. On the other hand, for the FMOF-1-OCH_3 and FMOF-1-CN structures, we notice a lower N_2 uptake over CO_2, while for the remaining structures vanishingly smaller N_2 uptake was observed compared to CO_2.

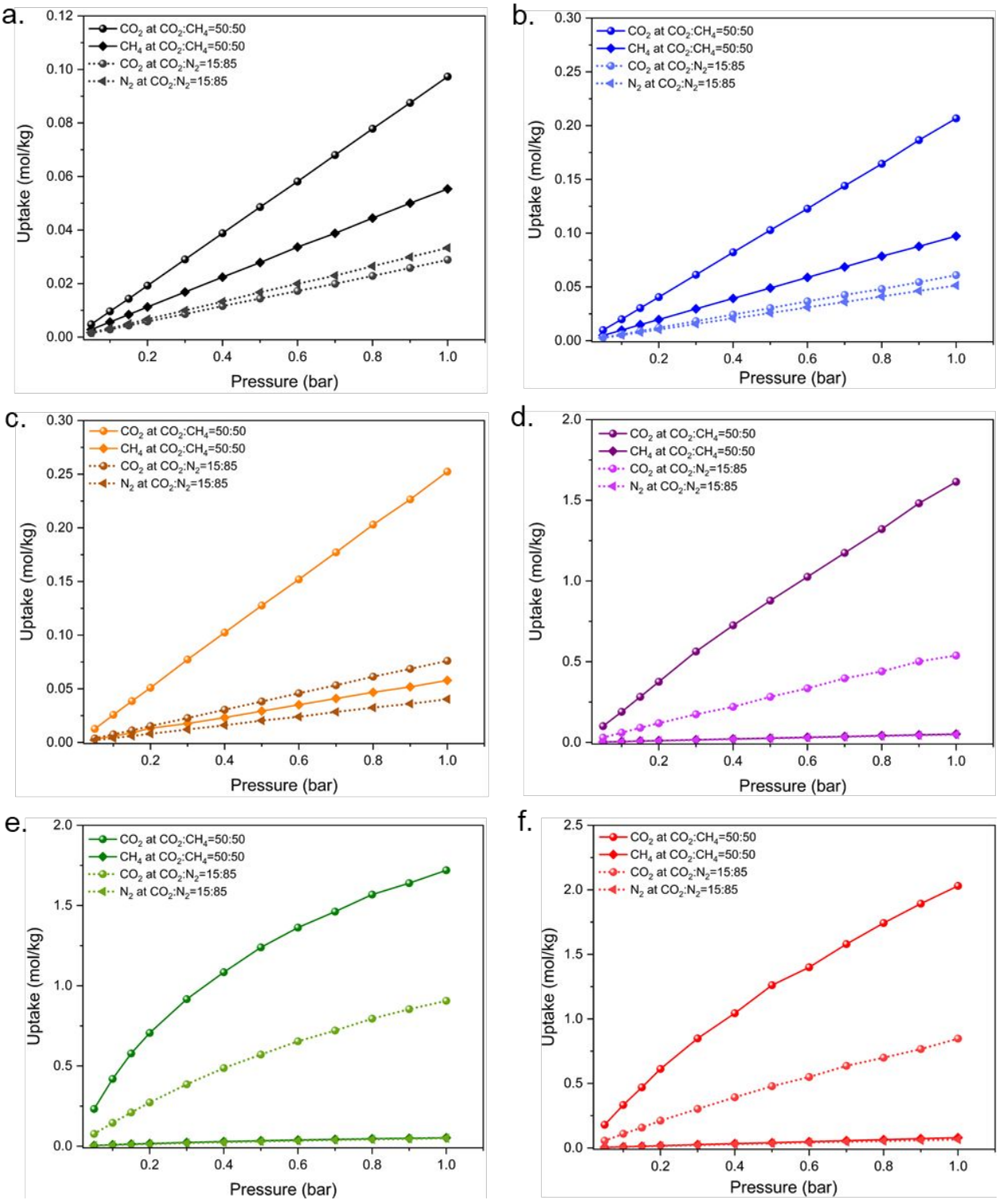

Figure 11. Adsorption isotherms of CO_2, CH_4, and N_2 for CO_2/CH_4 (50:50) and CO_2/N_2 (15:85) binary mixtures in (a) FMOF-1 (b) FMOF-1-OCH_3 (c) FMOF-1-CN (d) FMOF-1-OH (e) FMOF-1-COOH, and (f) FMOF-1-NH_2 at 298 K.

IAST was applied to calculate the adsorption selectivity of the MOF structures for the CO_2/CH_4 (50:50) and CO_2/N_2 (15:85) binary gas mixtures at 298 K (Figure 12). The selectivity values exhibit a similar trend for both the mixtures. All the X-functionalized structures exhibit higher selectivity values than that of the parent MOF structure. This could be attributed to the relatively stronger CO_2 interaction with the X-functionalized MOFs.[6] It is apparent that -OH, -COOH and -NH_2 functionalized MOFs significantly enhance the CO_2/CH_4 and CO_2/N_2 selectivities than the original FMOF-1. For CO_2/CH_4 gas mixture, the selectivity values were obtained as 59.6, 40.0 and 31.5, respectively, for the -COOH, -NH_2 and -OH functionalized MOFs at 0.1 bar pressure. These values are much higher compared to the values obtained from the -COOH, -NH_2 and -OH substituted MIL-53 (lp), where selectivity values are in the range of 12-17 at 0.1 bar.[29] For CO_2/N_2 gas mixture, FMOF-1-COOH exhibits the highest selectivity of 128.7 at 0.1 bar, which is higher than the dihydrofuran functional porous aromatic framework, DHF_PAF-1, having a value of 92.0 at infinite dilution.[6] For both the CO_2/CH_4 and CO_2/N_2 gas mixtures, we notice the selectivity values remain almost constant through the entire pressure range for FMOF-1, FMOF-1-OCH_3 and FMOF-1-CN structures. However, we observe the selectivity remains constant in all over the pressure range for FMOF-1, FMOF-1-OCH_3 and FMOF-1-CN. On the other hand, the selectivity gradually increases with the increasing pressure for FMOF-1-OH, FMOF-1-NH_2 and FMOF-1-COOH structures due to the amplified CO_2-CO_2 interactions at higher pressures.[70] We also compared the selectivity values of the CO_2/CH_4 and CO_2/N_2 gas mixtures, derived from the corresponding Henry's constant ratios with the values obtained by the IAST method, at 0.1 bar and 298 K. Details of this comparison can be found in the Electronic Supporting Information (ESI).

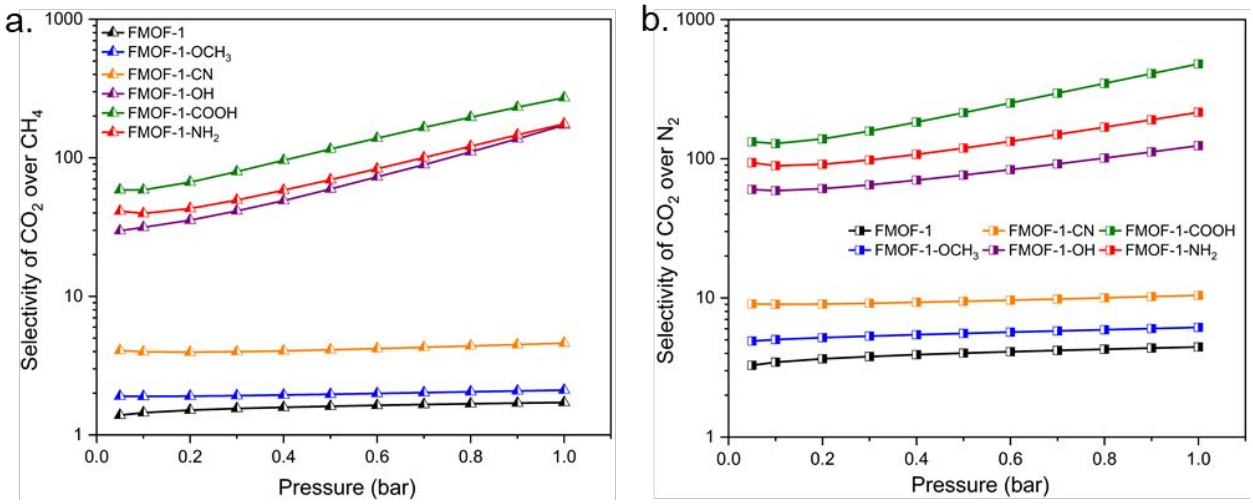

Figure 12. Adsorption selectivity for (a) CO_2/CH_4 and (b) CO_2/N_2 binary gas mixtures at 298 K, up to 1 bar.

3.6 Evaluation of the FMOFs for CO_2 separation

According to the adsorption evaluation criteria discussed earlier (Section 2.3), we assessed the potential of all the MOFs for CO_2 separation and capture. Tables 5 and 6 rank the MOFs for natural gas purification and landfill gas separation, respectively, in terms of their selectivity values.

Table 5: Comparison of MOFs for natural gas purification (CO_2/CH_4 = 10:90)

Structures	N^{ads} (mol/kg)	ΔN (mol/kg)	S
FMOF-1-OH	1.63	1.26	30.06
FMOF-1-NH_2	2.01	1.41	23.83
FMOF-1-COOH	1.74	1.13	22.66
FMOF-1-CN	0.25	0.20	4.67
FMOF-OCH_3	0.21	0.17	2.40
FMOF-1	0.10	0.08	1.94

For natural gas purification and landfill gas separation, the MOF structures follow the order of FMOF-1-OH > FMOF-1-NH_2 > FMOF-1-COOH > FMOF-1-CN > FMOF-1-OCH_3 > FMOF-1, obtained from the selectivity calculation as observed in Tables 5 and 6. Apparently, the selectivity values for the -OH functionalized MOF is 15.50 and 16.16 fold lager than that of the parent FMOF-

1 structure for natural gas purification and landfill gas separation, respectively. As shown in Table 5, FMOF-1-OH, FMOF-1-NH_2 and FMOF-1-COOH show relatively higher selectivity values (30.06, 23.83 and 22.66) compared to the remaining MOF structures. These values are higher than many materials for natural gas purification such as zeolite-5A (20.0), zeolite-13X (18.9), Mg-MOF-74 (17.3) and amine-MIL-53(Al) (16.7).[71] For landfill gas separation, the largest selectivity value was observed for -OH functionalized MOF (28.28). This value is comparable to NaY (30.0), but smaller than NaX (40.0).[72] Again, the selectivity values of -OH, -NH_2 and -COOH functionalized MOFs (28.28, 21.51 and 18.42) are higher than many MOFs, for example, Mg-MOF-74 (12.5), zeolite-13X (13.2) and zeolite-5A (23.5).[71,73] The presence of highly polar -OH, -NH_2 and -COOH functional groups in MOFs lead to the higher adsorption of quadrupolar CO_2 than that of the nonpolar CH_4 at the specified adsorption pressure, eventually results in larger selectivity values for the structures. Though FMOF-1-OH shows the largest selectivity value among all the structures, but FMOF-1-NH_2 seems to be the best adsorbent with respect to N^{ads} and working capacity (ΔN) performance. We speculate this higher N^{ads} and ΔN is due to the relatively larger pore volume of FMOF-1-NH_2 than the other structures.

Table 6: Comparison of MOFs for landfill gas separation (CO_2/CH_4 = 50:50)

Structures	N^{ads} (mol/kg)	ΔN (mol/kg)	S
FMOF-1-OH	1.63	1.44	28.28
FMOF-1-NH_2	2.01	1.68	21.51
FMOF-1-COOH	1.74	1.33	18.42
FMOF-1-CN	0.25	0.22	4.24
FMOF-OCH_3	0.21	0.19	2.10
FMOF-1	0.10	0.08	1.75

For flue gas separation, the MOF structures follow a different order of performance (Table 7) compared to the above two cases, in terms of selectivity. FMOF-1-COOH shows the highest selectivity value (71.70) among all the MOFs, which is larger than Ni-MOF-74 (41.1) and zeolite-5A (61.8),[71] but smaller than NaY (500).[72] For flue gas separation, a strong CO_2-MOF interaction is desired at low-pressure region, usually at 0.15 bar, that will lead to a very high CO_2 uptake. CO_2 shows the strongest interaction with FMOF-1-COOH as indicated by the largest CO_2 K_H value (Table 2). This results in the highest CO_2 uptake for the -COOH functionalized MOF at the stated adsorption pressure, 0.15 bar (Table 7). Nevertheless, FMOF-1-COOH exhibits a relatively smaller N_2 uptake (0.072 mol/kg) compared to FMOF-1-NH_2 (0.075 mol/kg) at 0.15 bar. Consequently, we notice the largest selectivity for FMOF-1-COOH among all the evaluated MOFs for flue gas separation.

Table 7: Comparison of MOFs for flue gas separation

Structures	N^{ads} (mol/kg)	ΔN (mol/kg)	S
FMOF-1-COOH	0.92	0.78	71.70
FMOF-1-NH_2	0.84	0.73	63.42
FMOF-1-OH	0.37	0.33	38.32
FMOF-1-CN	0.08	0.07	10.51
FMOF-OCH_3	0.06	0.05	6.68
FMOF-1	0.03	0.02	4.95

4. CONCLUSIONS

In this work, we have systematically investigated the effect of several de-fluorinating functional groups (X= -OCH_3, -CN, -OH, -COOH and -NH_2) on gas adsorption (CO_2, CH_4 and N_2) vs the parent FMOF-1 (X = -CF_3) up to a pressure of 30 bar. The Henry's constant (K_H) and isosteric heat of adsorption at infinite dilution (Q_{st0}) for CO_2 predicted via force field-based MC simulations

reveal enhanced interactions between CO_2 and the X-functionalized de-fluorinated MOFs. A greater CO_2 uptake at the low-pressure region (< 1 bar) is predicted for -OH, -COOH and -NH_2 functionalized structures compared to the -OCH_3, -CN functionalized structures. This finding suggests that the incorporation of polar functional groups to the linkers, containing lone pairs of electrons or acidic hydrogens can significantly enhance the CO_2 adsorption capacity of MOFs. However, at the high-pressure region, the adsorption properties of the MOFs are predominantly controlled by the structural properties of the materials, such as the free volume and the surface area, rather than the nature (polar or nonpolar) of the functional groups. This was verified by comparing all the gas uptake values of the MOF structures at 30 bar. The interaction energy values between CO_2 and -COOH/-OH/-NH_2 functionalized structures obtained by MP2 are qualitatively similar to that of the force-field based molecular simulation values. These interaction energies along with the radial distribution function of CO_2 around different functional groups provide information about the binding sites of CO_2 in the MOF structures investigated herein. The adsorption behavior of the multicomponent mixtures was predicted from the CO_2/CH_4 and CO_2/N_2 binary system, using GCMC simulations. FMOF-1-OH is predicted to show the highest selectivity for CO_2/CH_4, while the highest CO_2/N_2 adsorption selectivity was predicted to be for FMOF-1-COOH at room temperature. Adsorbent evaluation criteria data obtained for CO_2 separation indicates that -OH, -COOH and -NH_2 functionalized MOFs could be a promising class of porous materials for selective CO_2 capture. These findings represent a predictive step for new materials' development experimentally towards enhancement of CO_2 separation capability in particular needed for various technologies. A complementary investigation aimed at sustaining the super-hydrophobicity of FMOFs via CH_3 instead of CF_3 groups, hence reducing the water interference

(i.e., CO_2/H_2O and CH_4/H_2O selectivity instead of CO_2/CH_4 and CO_2/N_2 selectivity herein) is described elsewhere.

ASSOCIATED CONTENT

Electronic Supporting Information (ESI)

Electronic Supporting Information (ESI) is available free of cost at .....

AUTHOR INFORMATION

Corresponding Authors

Mohammad A. Omary - *Department of Chemistry, University of North Texas, 1155 Union Circle, Denton, Texas-76203, United States;*
orchid.org/0000-0002-3247-3449;
Email: Omary@unt.edu

Jincheng Du - *Department of Materials Science and Engineering, University of North Texas, 1155 Union Circle, Denton, Texas-76203, United States;*
orchid.org/0000-0003-4805-7498;
Email: Jincheng.du@unt.edu

Authors

Rashida Yasmeen - *Department of Materials Science & Engineering, University of North Texas, 1155 Union Circle, Denton, Texas-76203, United States;*
orchid.org/0000-0003-1637-0615

Sheikh M. S. Islam - *Department of Chemistry, University of North Texas, 1155 Union Circle, Denton, Texas-76203, United States;*
orchid.org/0000-0001-6909-7865

CONFLICT OF INTEREST

The authors report no conflict of interest of any kind.

DATA AVAILABILITY

The data supporting this article have been included as part of the Electronic Supplementary Information (ESI).

ACKNOWLEDGEMENTS

M.A.O. acknowledges support from the U.S. Nuclear Regulatory Commission (Award 31310023M0019), the U.S. Department of Defense (Award W911NF2210201), the Welch Foundation (B-1542), and the U.S. National Science Foundation (CHE-1413641 and an international supplement thereof, CHE-1545934). J.D. acknowledges support of his group's contribution from the U.S. National Science Foundation (CMMI-1662288) and in part by the Advanced Research Projects Agency-Energy (ARPA-E) of U.S. Department of Energy (DE AR0001613). The computational facilities have been supported by the National Science Foundation (CHE-1531468 and OAC-2117247) and the University of North Texas (Research Computing Services and Texas Advanced Computing Center). We also thank Prof. Randall Q. Snurr of Northwestern University/USA and Prof. Peyman Z. Moghadam of University College London/UK for providing access to the RASPA2 program (the latter also initial training and troubleshooting).

REFERENCES

1 R. Krishna, *The Journal of Physical Chemistry C*, 2009, **113**, 19756–19781.

2 R. Krishna and J. M. van Baten, *J Memb Sci*, 2010, **360**, 323–333.

3 L. Kong, R. Zou, W. Bi, R. Zhong, W. Mu, J. Liu, R. P. S. Han and R. Zou, *J. Mater. Chem. A*, 2014, **2**, 17771–17778.

4 J. McEwen, J.-D. Hayman and A. Ozgur Yazaydin, *Chem Phys*, 2013, **412**, 72–76.

5 C. Janiak and J. K. Vieth, *New Journal of Chemistry*, 2010, **34**, 2366.

6 R. Babarao, S. Dai and D. Jiang, *Langmuir*, 2011, **27**, 3451–3460.

7 J.-R. Li, J. Sculley and H.-C. Zhou, *Chem Rev*, 2012, **112**, 869–932.

8 K. J. Hartlieb, J. M. Holcroft, P. Z. Moghadam, N. A. Vermeulen, M. M. Algaradah, M. S. Nassar, Y. Y. Botros, R. Q. Snurr and J. F. Stoddart, *J Am Chem Soc*, 2016, **138**, 2292–2301.

9 J. Hu, Y. Liu, J. Liu and C. Gu, *AIChE Journal*, DOI:10.1002/aic.16835.

10 Z. Zhang, Z.-Z. Yao, S. Xiang and B. Chen, *Energy Environ Sci*, 2014, **7**, 2868.

11 T. Düren, L. Sarkisov, O. M. Yaghi and R. Q. Snurr, *Langmuir*, 2004, **20**, 2683–2689.

12 J.-R. Li, R. J. Kuppler and H.-C. Zhou, *Chem Soc Rev*, 2009, **38**, 1477.

13 R. J. Kuppler, D. J. Timmons, Q.-R. Fang, J.-R. Li, T. A. Makal, M. D. Young, D. Yuan, D. Zhao, W. Zhuang and H.-C. Zhou, *Coord Chem Rev*, 2009, **253**, 3042–3066.

14 V. Finsy, S. Calero, E. García-Pérez, P. J. Merkling, G. Vedts, D. E. De Vos, G. V. Baron and J. F. M. Denayer, *Physical Chemistry Chemical Physics*, 2009, **11**, 3515.

15 D. M. D'Alessandro, B. Smit and J. R. Long, *Angewandte Chemie International Edition*, 2010, **49**, 6058–6082.

16 X.-J. Wang, P.-Z. Li, Y. Chen, Q. Zhang, H. Zhang, X. X. Chan, R. Ganguly, Y. Li, J. Jiang and Y. Zhao, *Sci Rep*, 2013, **3**, 1149.

17 X. Liu, M. Park, S. Hong, M. Oh, J. W. Yoon, J.-S. Chang and M. S. Lah, *Inorg Chem*, 2009, **48**, 11507–11509.

18 S. Li, Y. G. Chung, C. M. Simon and R. Q. Snurr, *J Phys Chem Lett*, 2017, **8**, 6135–6141.

19 M. Eddaoudi, J. Kim, N. Rosi, D. Vodak, J. Wachter, M. O'Keeffe and O. M. Yaghi, *Science (1979)*, 2002, **295**, 469–472.

20 Y. H. Jhon, M. Cho, H. R. Jeon, I. Park, R. Chang, J. L. C. Rowsell and J. Kim, *The Journal of Physical Chemistry C*, 2007, **111**, 16618–16625.

21 T. Sagara, J. Klassen, J. Ortony and E. Ganz, *J Chem Phys*, DOI:10.1063/1.1944730.

22 J. R. Karra and K. S. Walton, *The Journal of Physical Chemistry C*, 2010, **114**, 15735–15740.

23 K. K. Tanabe and S. M. Cohen, *Chem. Soc. Rev.*, 2011, **40**, 498–519.

24 J. Hu, Y. Liu, J. Liu and C. Gu, *Fuel*, 2017, **200**, 244–251.

25 B. Arstad, H. Fjellvåg, K. O. Kongshaug, O. Swang and R. Blom, *Adsorption*, 2008, **14**, 755–762.

26 J. An, S. J. Geib and N. L. Rosi, *J Am Chem Soc*, 2010, **132**, 38–39.

27 S. Couck, J. F. M. Denayer, G. V. Baron, T. Rémy, J. Gascon and F. Kapteijn, *J Am Chem Soc*, 2009, **131**, 6326–6327.

28 B. Zheng, J. Bai, J. Duan, L. Wojtas and M. J. Zaworotko, *J Am Chem Soc*, 2011, **133**, 748–751.

29 A. Torrisi, R. G. Bell and C. Mellot-Draznieks, *Cryst Growth Des*, 2010, **10**, 2839–2841.

30 A. Torrisi, R. G. Bell and C. Mellot-Draznieks, *Microporous and Mesoporous Materials*, 2013, **168**, 225–238.

31 C. Gu, Y. Liu, W. Wang, J. Liu and J. Hu, *Front Chem Sci Eng*, 2021, **15**, 437–449.

32 A. Torrisi, C. Mellot-Draznieks and R. G. Bell, *J Chem Phys*, DOI:10.1063/1.3120909.

33 K. D. Vogiatzis, A. Mavrandonakis, W. Klopper and G. E. Froudakis, *ChemPhysChem*, 2009, **10**, 374–383.

34 A. Torrisi, C. Mellot-Draznieks and R. G. Bell, *J Chem Phys*, DOI:10.1063/1.3276105.

35 T. Düren, Y.-S. Bae and R. Q. Snurr, *Chem Soc Rev*, 2009, **38**, 1237.

36 D. H. Jung, D. Kim, T. B. Lee, S. B. Choi, J. H. Yoon, J. Kim, K. Choi and S.-H. Choi, *J Phys Chem B*, 2006, **110**, 22987–22990.

37 A. Martín-Calvo, E. García-Pérez, J. Manuel Castillo and S. Calero, *Physical Chemistry Chemical Physics*, 2008, **10**, 7085.

38 T. Sagara, J. Klassen and E. Ganz, *J Chem Phys*, 2004, **121**, 12543–12547.

39 C. Yang, X. Wang and M. A. Omary, *J Am Chem Soc*, 2007, **129**, 15454–15455.

40 P. Z. Moghadam, J. F. Ivy, R. K. Arvapally, A. M. dos Santos, J. C. Pearson, L. Zhang, E. Tylianakis, P. Ghosh, I. W. H. Oswald, U. Kaipa, X. Wang, A. K. Wilson, R. Q. Snurr and M. A. Omary, *Chem Sci*, 2017, **8**, 3989–4000.

41 *Material Studio Modeling Environment, Release 6, Accelrys Software Inc., San Diego, California, USA, 2011.*

42 D. A. Gomez-Gualdron, O. V. Gutov, V. Krungleviciute, B. Borah, J. E. Mondloch, J. T. Hupp, T. Yildirim, O. K. Farha and R. Q. Snurr, *Chemistry of Materials*, 2014, **26**, 5632–5639.

43 O. K. Farha, A. Özgür Yazaydın, I. Eryazici, C. D. Malliakas, B. G. Hauser, M. G. Kanatzidis, S. T. Nguyen, R. Q. Snurr and J. T. Hupp, *Nat Chem*, 2010, **2**, 944–948.

44 O. V. Gutov, W. Bury, D. A. Gomez-Gualdron, V. Krungleviciute, D. Fairen-Jimenez, J. E. Mondloch, A. A. Sarjeant, S. S. Al-Juaid, R. Q. Snurr, J. T. Hupp, T. Yildirim and O. K. Farha, *Chemistry – A European Journal*, 2014, **20**, 12389–12393.

45 A. K. Rappe, C. J. Casewit, K. S. Colwell, W. A. Goddard and W. M. Skiff, *J Am Chem Soc*, 1992, **114**, 10024–10035.

46 T. F. Willems, C. H. Rycroft, M. Kazi, J. C. Meza and M. Haranczyk, *Microporous and Mesoporous Materials*, 2012, **149**, 134–141.

47 D. Dubbeldam, S. Calero, D. E. Ellis and R. Q. Snurr, *Mol Simul*, 2016, **42**, 81–101.

48 M. Sedighi, M. R. Talaie, H. Sabzyan, S. Aghamiri and P. Chen, *Fuel*, 2022, **308**, 121965.

49 K. Sladekova, C. Campbell, C. Grant, A. J. Fletcher, J. R. B. Gomes and M. Jorge, *Adsorption*, 2020, **26**, 663–685.

50 P. P. Ewald, *Ann Phys*, 1921, **369**, 253–287.

51 J. J. Potoff and J. I. Siepmann, *AIChE Journal*, 2001, **47**, 1676–1682.

52 M. G. Martin and J. I. Siepmann, *J Phys Chem B*, 1998, **102**, 2569–2577.

53 *D. Frenkel and B. Smit, Understanding Molecular Simulation: From algorithm to Applications, Elsevier Inc., 2023.*

54 B. Widom, *J Chem Phys*, 1963, **39**, 2808–2812.

55 T. J. H. Vlugt, E. García-Pérez, D. Dubbeldam, S. Ban and S. Calero, *J Chem Theory Comput*, 2008, **4**, 1107–1118.

56 J. Baker, *J Comput Chem*, 1986, **7**, 385–395.

57 Gaussian 16, Revision C.01, M. J. Frisch, G. W. Trucks, H. B. Schlegel, G. E. Scuseria, M. A. Robb, J. R. Cheeseman, G. Scalmani, V. Barone, G. A. Petersson, H. Nakatsuji, X. Li, M. Caricato, A. V. Marenich, J. Bloino, B. G. Janesko, R. Gomperts, B. Mennucci, H. P. Hratchian, J. V. Ortiz, A. F. Izmaylov, J. L. Sonnenberg, D. Williams-Young, F. Ding, F. Lipparini, F. Egidi, J. Goings, B. Peng, A. Petrone, T. Henderson, D. Ranasinghe, V. G. Zakrzewski, J. Gao, N. Rega, G. Zheng, W. Liang, M. Hada, M. Ehara, K. Toyota, R. Fukuda, J. Hasegawa, M. Ishida, T. Nakajima, Y. Honda, O. Kitao, H. Nakai, T. Vreven, K. Throssell, J. A. Montgomery, Jr., J. E. Peralta, F. Ogliaro, M. J. Bearpark, J. J. Heyd, E. N. Brothers, K. N. Kudin, V. N. Staroverov, T. A. Keith, R. Kobayashi, J. Normand, K. Raghavachari, A. P. Rendell, J. C. Burant, S. S. Iyengar, J. Tomasi, M. Cossi, J. M. Millam, M. Klene, C. Adamo, R. Cammi, J. W. Ochterski, R. L. Martin, K. Morokuma, O. Farkas, J. B. Foresman, and D. J. Fox, Gaussian, Inc., Wallingford CT, 2016.

58 C. Altintas, G. Avci, H. Daglar, A. Nemati Vesali Azar, S. Velioglu, I. Erucar and S. Keskin, *ACS Appl Mater Interfaces*, 2018, **10**, 17257–17268.

59 A. L. Myers and J. M. Prausnitz, *AIChE Journal*, 1965, **11**, 121–127.

60 L. Qu, Z. Wang and L. Liu, *Fire*, 2023, **6**, 355.

61 P. Chowdhury, S. Mekala, F. Dreisbach and S. Gumma, *Microporous and Mesoporous Materials*, 2012, **152**, 246–252.

62 Z. Cai, C. E. Bien, Q. Liu and C. R. Wade, *Chemistry of Materials*, 2020, **32**, 4257–4264.

63 S. R. Caskey, A. G. Wong-Foy and A. J. Matzger, *J Am Chem Soc*, 2008, **130**, 10870–10871.

64 S. Cavenati, C. A. Grande and A. E. Rodrigues, *J Chem Eng Data*, 2004, **49**, 1095–1101.

65 K. S. Walton, M. B. Abney and M. Douglas LeVan, *Microporous and Mesoporous Materials*, 2006, **91**, 78–84.

66 S. M. S. Islam, R. Yasmeen, G. Verma, S. M. Tekarli, V. N. Nesterov, S. Ma and M. A. Omary, *Inorg Chem*, 2024, **63**, 8664–8673.

67 H. W. B. Teo, A. Chakraborty and S. Kayal, *Appl Therm Eng*, 2017, **110**, 891–900.

68 R. Ahlrichs, M. Bär, M. Häser, H. Horn and C. Kölmel, *Chem Phys Lett*, 1989, **162**, 165–169.

69 Z. Xiang, S. Leng and D. Cao, *The Journal of Physical Chemistry C*, 2012, **116**, 10573–10579.

70 Y. Chen and J. Jiang, *ChemSusChem*, 2010, **3**, 982–988.

71 Y. Bae and R. Q. Snurr, *Angewandte Chemie International Edition*, 2011, **50**, 11586–11596.

72 R. Krishna and J. M. van Baten, *Physical Chemistry Chemical Physics*, 2011, **13**, 10593.

73 D. Saha, Z. Bao, F. Jia and S. Deng, *Environ Sci Technol*, 2010, **44**, 1820–1826.

DATA AVAILABILITY

The data supporting this article have been included as part of the Electronic Supplementary Information (ESI).